Refinement strategies for optimal inclusion of prior information in ptychography

Ansuinelli, Paolo; Coene, Wim M.; Urbach, H. P.

DOI
10.1117/12.2572019

Publication date
2020

Document Version
Final published version

Published in
Extreme Ultraviolet Lithography 2020

Citation (APA)
Ansuinelli, P., Coene, W. M., & Urbach, H. P. (2020). Refinement strategies for optimal inclusion of prior information in ptychography. In P. P. Naulleau, P. A. Gargini, T. Itani, & K. G. Ronse (Eds.), *Extreme Ultraviolet Lithography 2020* (Vol. 11517). Article 1151711 (Proceedings of SPIE - The International Society for Optical Engineering; Vol. 11517). SPIE. https://doi.org/10.1117/12.2572019

PROCEEDINGS OF SPIE

SPIEDigitalLibrary.org/conference-proceedings-of-spie

Refinement strategies for optimal inclusion of prior information in ptychography

Ansuinelli, Paolo, Coene, Wim, Urbach, H.

Paolo Ansuinelli, Wim M.J.M. Coene, H. P. Urbach, "Refinement strategies for optimal inclusion of prior information in ptychography," Proc. SPIE 11517, Extreme Ultraviolet Lithography 2020, 1151711 (20 September 2020); doi: 10.1117/12.2572019

SPIE.

Event: SPIE Photomask Technology + EUV Lithography, 2020, Online Only

Refinement strategies for optimal inclusion of prior information in ptychography

Paolo Ansuinelli[a], Wim M.J.M. Coene[a,b], and H.P. Urbach[a]

[a]Optics Research Group, Department of Imaging Physics, Faculty of Applied Sciences, Delft University of Technology, P.O. Box 5046, 2600 GA Delft, The Netherlands
[b]ASML Netherlands B.V., De Run 6501, 5504 DR Veldhoven, The Netherlands

ABSTRACT

The imaging and inspection of extreme ultraviolet (EUV) masks is an important aspect of EUV lithography. The availability of actinic mask inspection tools able to generate highly resolved defect maps of defective EUV layouts is needed to ensure defect–free wafer prints. The technological interest towards phase–shift absorber materials for the next generation of EUV masks, and the associated need for phase metrology at the absorber level, makes phase retrieval methods a particularly interesting option for actinic inspection. In this work we use ptychography as an inspection tool for EUV masks. We show how variational and statistical methods can be employed to include *a–priori* information in the ptychographic inverse problem and how to cluster different update rules – stemming from the minimization of appropriate cost functionals – to optimally include prior information in ptychography under Poisson noise.

Keywords: EUV lithography, mask inspection, phase retrieval, optimization, prior information, ptychography

1. INTRODUCTION

The characterization and inspection of EUV masks is necessary to ensure the printing of defect–free wafers in EUV lithography. The importance of actinic inspection and the necessity of methods for phase metrology of EUV absorbers, e.g. in view of the of the possible use of attenuated phase–shift masks for next generation EUV lithography,[1] makes actinic phase imaging microscopes particularly appealing.

Ptychography[2] is a widely employed lensless imaging method which employs a diverse and redundant data set to retrieve a highly resolved wide–field–of–view image of a given object via phase retrieval. Research in ptychography comprises algorithm development and experimental work for novel measurement and detection schemes.

Ptychography has advanced enormously since its early introduction and now it comprises – among other developments – schemes for probe retrieval[3–5] , advanced optimization methods for denoising,[6,7] proximal algorithms for optimization,[8] methods for reconstruction of 3–D samples,[9] tomographic reconstruction of samples,[10] implementation with visible and X–ray light of Fourier ptychography[11,12] and schemes with speckle illuminations[13] to mention a few.

Experimental work for the imaging of structures in reflective setups at short wavelength has been the subject of recent studies.[14,15] The use of this coherent diffractive imaging method as a tool for EUV layout inspection has also been investigated and discussed.[16–18] In[19] we have computationally shown how the availability of prior information in lithography, present in the form of the nominal mask layout as in a typical GDS mask design file, can be employed to improve the detectability of fine defects. Given a certain *a–priori* known scattering geometry the exit wave was rigorously computed and appropriately processed to give a prior for the reflection function of the object. This in turn enabled the inspection and imaging of finer defects with respect to the result given by the application of the standard ptychographic iterative engine (PIE). The main goal of this paper is to deepen the study we performed in[19] by showing how to combine certain update rules to optimally include prior information in ptychography for the purpose of defect inspection and imaging under Poisson noise.

E-mail: p.ansuinelli@tudelft.nl

Extreme Ultraviolet Lithography 2020, edited by Patrick P. Naulleau, Paolo A. Gargini, Toshiro Itani, Kurt G. Ronse, Proc. of SPIE Vol. 11517, 1151711 · © 2020 SPIE · CCC code: 0277-786X/20/$21 · doi: 10.1117/12.2572019

2. METHODS

In the ptychographic method a probe, $P(\mathbf{r})$, sequentially illuminates different parts a certain object, $O(\mathbf{r})$, at partially overlapping probe positions. The exit wave is assumed to be given by the Hadamard product among the probe and the object and it is propagated to a detector which is usually located at the far–field. The exit wave in the object space is then related to the far–field by a Fourier transform as a result of Fraunhofer diffraction. The phase problem originates by the impossibility to directly measure the phase in optical set–ups. Ptychography can be seen as a cost functional minimization problem:

$$\begin{aligned} \mathcal{L}(O, I_{m,j}) &\coloneqq \left|\left| |\mathcal{F}(P(\mathbf{r}-\mathbf{R}_j)O(\mathbf{r}))| - \sqrt{I_{m,j}(\mathbf{k})} \right|\right|^2 \\ O(\mathbf{r}) &\coloneqq \arg\min_{O} \mathcal{L}(O, I_{m,j}) \end{aligned} \tag{1}$$

where $\mathcal{F}$ represents the Fourier transform, $P(\mathbf{r})$ is the probe function, $O(\mathbf{r})$ is the part of the guessed object which is illuminated when the probe is located at the j–th probe position and $I_{m,j}(\mathbf{k})$ is the intensity pattern measured at the j–th probe position. In (1) and in all that follows we assume the probe to be known. The PIE proceeds in a sequential fashion and the complete object, $O(\mathbf{r})$, is reconstructed from the sequential reconstruction of its j-th views.[2] In our prior work[19] we demonstrated that the inclusion of prior information in Eq.(1) improves the solution to the point where smaller defects get revealed in the reconstructed object. More precisely we minimized, per probe position, the following cost functional:

$$\begin{aligned} \mathcal{L}^{\alpha}(O, I_j) &\coloneqq \mathcal{L}(O, I_j) + R^{\alpha}(O) = \\ &= \left|\left| |\mathcal{F}(P(\mathbf{r}-\mathbf{R}_j)O(\mathbf{r}))| - \sqrt{I_{m,j}(\mathbf{k})} \right|\right|^2 + \alpha \left|\left| O(\mathbf{r}) - O_p(\mathbf{r}) \right|\right|^2 \end{aligned} \tag{2}$$

where α regulates the interplay among the two terms on the right hand side of Eq. (2). The second term in (2) penalizes large deviations of the reconstructed object from the prior object $O_p(\mathbf{r})$. More details on how the prior object O_p is computed are given in the next section. The cost functional in Eq. (2) can be thought of as an approximation of the maximum likelihood method for Poisson noise.[20]

It is common practice in the phase retrieval community to cluster different update rules and different methods together in order to avoid stagnation and achieve a better reconstruction.[12,20,21] In the following we present cost functionals that we have found to enable better reconstructions when combined with the update rule given by the minimization of Eq. (2) in presence of Poisson noise.

2.1 Maximum a posteriori estimation

The tools offered by statistical regularization theory can be employed to derive a cost functional that accounts for the knowledge of both the noise model and the prior information. If photon counting is the main source of noise in the physical set–up then the number of photons detected follows the Poissonian statistics. The detected number of photons at the j–th probe position, $n_{m,j}$ is interrelated to the measured intensities $I_{m,j}$ by:

$$n_{m,j} = \frac{I_{m,j}}{h\nu} \quad \text{where} \quad \nu = \frac{v}{\lambda} \tag{3}$$

where h is the Plank's constant, ν is the frequency, λ is the wavelength and v is the light speed within a certain medium. If we assume the incoming light beam to be monochromatic the intensity distribution will also be Poissonian and, at the j–th probe position, the probability of measuring a certain number of photons $n_{m,j}$, given a certain object $O(\mathbf{r})$, will be given by the likelihood:[20]

$$L(O) \coloneqq p(n_{m,j}, O) = \prod_{\mathbf{k}} \frac{I_j(\mathbf{k})^{n_{m,j}(\mathbf{k})}}{n_{m,j}(\mathbf{k})!} e^{-I_j(\mathbf{k})}. \tag{4}$$

where $I_j(\mathbf{k})$ is the guessed intensity as given by $I_j = |\mathcal{F}(P(\mathbf{r}-\mathbf{R}_j))O(\mathbf{r})|^2$. Following Bayes theorem we can introduce, given Eq. (4) and a prior distribution for the model parameters, the posterior:

$$\pi_{post}(O|n_{m,j}) = \frac{L(O)\pi_{prior}(O)}{\int L(O)\pi_{prior}(O)dO} \tag{5}$$

where π_{prior} represents the prior distribution. We assume the prior distribution to be a complex valued Gaussian peaked at a certain prior object O_p:

$$\pi_{prior}(O) = \frac{e^{-(O-O_p)^H\Gamma^{-1}(O-O_p)}}{|\pi\Gamma|} = \frac{1}{\pi\sigma^2}\exp\left[\frac{-|O-O_p|^2}{\sigma^2}\right] \tag{6}$$

where H denotes the Hermitan transpose and Γ is a Hermitian positive definite matrix that contains the complex variance. We assumed in Eq. (6) that Γ is diagonal with equal real elements given by σ^2. We notice that the standard deviation in Eq. (6) essentially plays the role of the regularization parameter. The reconstruction of the full posterior distribution in Eq. (5) is extremely computationally demanding, and it is common to retrieve from it only point estimators that are statistically relevant. The maximum–a–posteriori (MAP) estimator is defined as the value of the to be retrieved parameter that maximizes (5):

$$O_{MAP} = \arg\max_O \pi_{post}(O|n_{m,j}) = \arg\min_O\{-logL(O) - log\pi_{prior}(O)\} = \arg\min_O \mathcal{L}_{MAP}(O, n_{m,j}) \tag{7}$$

The update of the object reflection function at the j–th probe position will be given by:

$$O_{MAP} = \arg\min\left\{\sum_{\mathbf{k}}[I_j(\mathbf{k}) - n_{m,j}(\mathbf{k})log(I_j(\mathbf{k}))] + \sum_{\mathbf{r}}\frac{1}{\sigma^2}|O(\mathbf{r}) - O_p(\mathbf{r})|^2\right\} \tag{8}$$

where we have left out constant terms. In Eq. (8) $\mathbf{k}$ runs over the pixels in the Fourier space and $\mathbf{r}$ over the pixels in real space. The prior O_p is the same than the one we used in.[19] More specifically, owing to high 3 dimensional complexity of the scattering geometry, the prior object is accurately generated by computing the exit–wave recurring to Maxwell solvers by means of which the light–matter interaction is computed by solving rigorously Maxwell's equations. The intrinsically different modeling in light–sample interaction in ptychography and in the Maxwell solver could be a reason of concern when intermixing the two methods and care should be taken when attempting to do so. In other words, a certain rigorously computed complex-valued far-field, Ψ^{Maxw}, can be used in ptychographic algorithms only when it can be interpreted in terms of the 2D ptychographic approximation of light—matter interaction

$$\Psi^{Maxw}_{p,j} \approx \mathcal{F}(P(\mathbf{r}-\mathbf{R}_j)O_p(\mathbf{r})) \tag{9}$$

where $\Psi^{Maxw}_{p,j}$ is the far–field, amplitude and phase, as computed by the forward Maxwell solver, for the nominal – *a priori* known – scattering geometry on the mask. Notice that although ptychography assumes the object function to be two–dimensional, $\Psi^{Maxw}_{p,j}$ is computed by the rigorous 3D simulations. When Eq. (9) holds it is possible for us to retrieve the prior for the transmission/reflection function of the object from the rigorously computed far–field: $O_p = P^*\frac{\mathcal{F}^{-1}(\Psi^{Maxw}_{p,j})}{|P|^2}$.

Eq. (8) can be minimized analytically and, when including (9), the gradient descent rule reads:

$$\begin{aligned} O_{MAP,n+1} = O_n - \beta\nabla\mathcal{L}_{MAP}(O, I_j) = O_n + \beta\frac{|P_j|}{|P_{j,max}|}\frac{P_j^*}{(|P_j|^2+c)}\mathcal{F}^{-1}(\frac{n_{m,j}}{I_j}\Psi_{j,n} - \Psi_{j,n}) \\ + \alpha\frac{|P_j|}{|P_{j,max}|}\frac{P_j^*}{(|P_j|^2+c)}\mathcal{F}^{-1}(\Psi^{Maxw}_{p,j} - \Psi_{j,n}) \end{aligned} \tag{10}$$

where $\Psi_{j,n} = \mathcal{F}(P(\mathbf{r}-\mathbf{R}_j)O(\mathbf{r}))$, $\alpha = \beta/\sigma^2$ and the factor $|P_j|^2$ at the denominator needs to be included so that Eq. (10) has the dimensions of an object.

2.2 Iteratively refined regularizer

In the section above we have changed the update rule so to incorporate the knowledge of the noise model and we have introduced an assumed prior distribution for the model parameters to derive a certain update rule from statistical considerations. Another interesting update could be obtained by employing the update rule that stems from the minimization of Eq. (2) followed by the minimizer of

$$\mathcal{L}_{IR}(O, I_{m,j}) = \left\| |\mathcal{F}(P(\mathbf{r}-\mathbf{R}_j)O(\mathbf{r}))| - \sqrt{I_{m,j}(\mathbf{k})} \right\|^2 + \alpha \left|\left|O(\mathbf{r}) - O_{n-1}(\mathbf{r})\right|\right|^2 \tag{11}$$

where the subscript IR stresses the fact that the regularization weight is changed iteratively. The reasoning behind this proposal is intuitive. As the optimization proceeds, and once it has reached or it is close to reach convergence, the retrieved solution at the previous iteration will be closer to the ground truth than the prior O_p in Eq. (2). Therefore one could think to penalize large deviations of the object reflection function with respect to O_{n-1} rather than O_p. In other words we are seeking to introduce a regularizer that is closer to the true solution than $O_p(\mathbf{r})$. The update rule in this case will read:

$$\begin{aligned} O_{IR,n+1} = O_n - \beta \nabla \mathcal{L}_{IR}(O, I_j) = O_{j,n} &+ \beta \frac{|P_j|}{|P_{j,max}|} \frac{P_j^*}{(|P_j|^2 + c)} \mathcal{F}^{-1}(\Psi_{c,j,n} - \Psi_{j,n}) \\ &+ \alpha' \frac{|P_j|}{|P_{j,max}|} \frac{P_j^*}{(|P_j|^2 + c)} \mathcal{F}^{-1}(\Psi_{j,n-1} - \Psi_{j,n}) \end{aligned} \tag{12}$$

where $\alpha' = \alpha\beta$ and $\Psi_{c,j,n}$ is the revised or corrected wavefront obtained by replacing the guessed amplitudes with the measured ones.

3. RESULTS

In what follows we apply the methods outlined above to the reconstruction of defective EUV mask layouts. The data set is the same we used previously,[19] but corrupted with Poisson noise.

3.1 Materials and masks

Material properties and thicknesses we have used throughout this work are outlined in Table 1.

Table 1: **Layers thicknesses and Materials at $\lambda = 13.5$ nm**

layer	thickness [nm]	n	k
ARC TaBO	2	0.952	0.026
Absorber TaBN	58	0.95	0.031
Ru	0.5	0.88586	0.01727
Ru (Capping layer)	2	0.88586	0.01727
Si	1.8968	0.99888	0.00183
MoSi2	0.7986	0.96908	0.00435
Mo	2.496	0.92347	0.00649
MoSi2	1.8908	0.96908	0.00435

Four EUV masks have been considered through this study:

- the “nominal” mask. This is the structure or cell as given by prior information. This cell does not contain any information about the defects.
- The “actual” mask. This is the cell that mimics the “reference” mask which is close to the prior but not exactly the same. In order to account for this difference the actual cell has been generated from the prior or nominal cell, displacing the sides of the polygons over a length of 1–5 nm. This cell is displayed in Fig. 1(a).

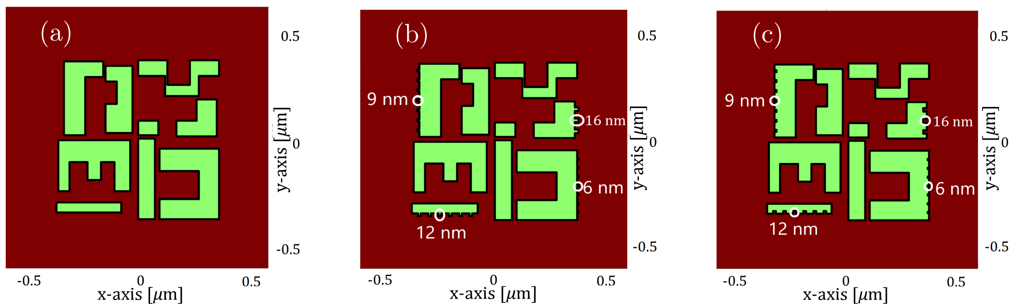

Figure 1: Top views of EUV mask layouts. a) Actual cell , b) programmed defect mask (extrusions), c) programmed defect mask (intrusions). The sidelength of the single defect is specified in the figure.

- The programmed defects mask. Consistently with the practice in EUV mask defectivity studies we have perturbed the absorber of the actual mask, at known locations, with additive and subtractive features (extrusions and intrusion defects) (Figs. 1(b–c))

The size of the defects in Figs. 1(b,c) is the same on a given polygon, and it changes from polygon to polygon. The number and the side length of the squares that constitute the rough extrusions/intrusions on a certain polygon are the following: [*number of squares*, *side length*] = [3, 16 nm], [6, 12 nm], [7, 9 nm], [7, 6 nm]. Such sizes have been chosen in accordance to the theoretical Abbe resolution limit given by $\lambda/(2NA)$ where we have chosen NA = 0.6 for wich the Abbe limit equals 11 nm.

The data–set relative to each of the four masks described above has been generated via fully rigorous 3D simulations using a volume–integral Maxwell solver.[22,23] The probe is assumed to be a Gaussian beam with a 3σ amplitude of about 1.5 μm and it is described by its angular spectrum. The scattered far–field is evaluated, for each of the plane waves which compose the illumination, in parallel on a multicore HPC cluster. The output far–field that results from the interaction of the probe with the object is then given by the weighed coherent superposition of the individual contributions. The ptychographic scans are performed by shifting the object of 0.2 μm, in 5 positions, inside the supercell. The probe is polarized in the x direction – parallel to the horizontal axis of the supercell – by proper linear combination of s and p polarization states. The photon flux is $5e11$ photons per unit time.

To understand whether the use of Eqs.(10) and (12) yield any benefits for our specific application we have carried out a computational die–to–database comparison.[24] This is done comparing the reconstruction of the defected mask with the reconstruction of the defect–free actual mask. The two reconstructions are subtracted one from the other to identify the defects at their locations. The impact of the defects is quantified by a certain figure of merit. In what follows we will use the defect SNR defined as:

$$SNR = \frac{\bar{A}_d - \bar{A}_a}{std(A_a)} \tag{13}$$

Where $\bar{A}_d$ is the average magnitude of the defected area, $\bar{A}_a$ is the average magnitude of the whole difference image – where the object is present – and $std(A_a)$ is the standard deviation of the latter area. The definition of the defect SNR is independent of the defect size. This investigation is done using the PIE with prior[19] followed by the update given by Eq. (10) or the one in Eq. (12).

3.2 Extrusion defects

Figure 2 highlights reconstructions in magnitude and phase for extrusion typed defects. We have reconstructed using 600 iterations with the method presented in our previous work followed by 200 iterations of either Eq. (10) or (12).

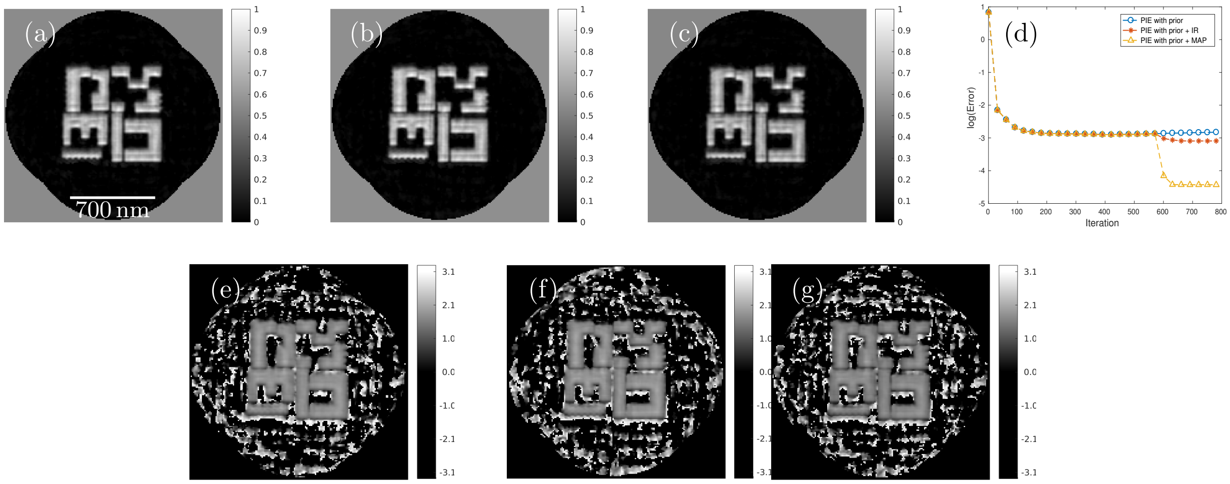

Figure 2: Ptychographic reconstructions: a) magnitude as given by the MAP, Eq. (10); b) magnitude given by the iteratively refined regularization weight, Eq. (12); c) magnitude given by the PIE with prior information; d) error in the far field; e)–g) phase relative to Figs. a)–c)

The outcome of the die–to–database inspection is given below.

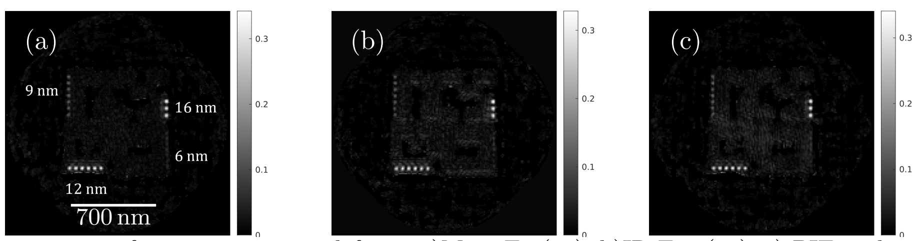

Figure 3: Difference images for extrusion type defects. a)Map, Eq.(10), b)IR Eq. (12), c) PIE with prior information

The defects' SNR, defined in Eq. (13), is reported in Table 2:

Table 2: **Extrusions defects SNR**

Defect Size [nm]	MAP (5 probe positions)	IR	Prior PIE
16	5.2	4.8	4.7
12	6.7	5.1	5.2
9	3.5	2	2

3.3 Intrusion defects

Figure 4 highlights reconstructions in magnitude and phase for intrusion type defects. The reconstruction proceeded as discussed in the previous section.

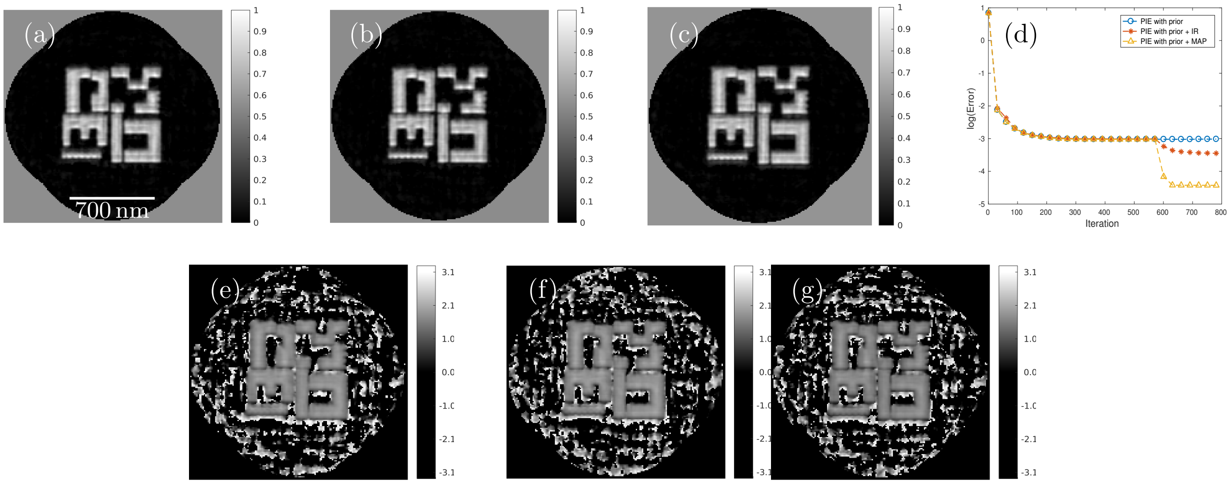

Figure 4: Ptychographic reconstructions: a) magnitude as given by the MAP, Eq. (10); b) magnitude given by the iteratively refined regularization weight, Eq. (12); c) magnitude given by the PIE with prior information; d) error in the far field; e)–g) phase relative to Figs. a)–c)

The difference images are given below.

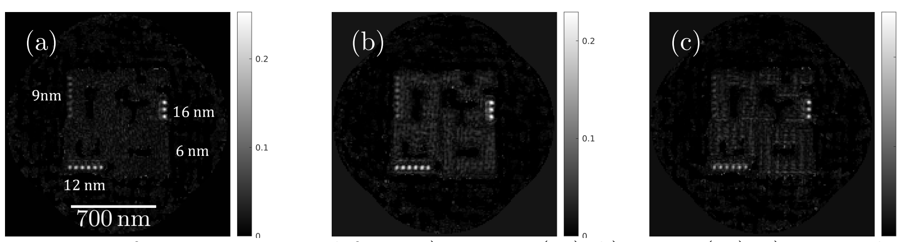

Figure 5: Difference images for intrusion type defects. a)Map, Eq.(10), b)IR Eq. (12), c) PIE with prior information

The defects SNR are reported below

Table 3: **Intrusion defects SNR**

Defect Size [nm]	MAP (5 probe positions)	IR	Prior PIE
16	5	5.2	3.5
12	5	4.6	3.4
9	3.5	2	2

3.4 Comparison with a sparsity prior for the object

As the object covers a small part of the reconstruction matrix it is interesting to compare results with the one given by a sparsity constraint for the object. We solve, per probe position, the following problem via the alternating direction method of multiplier:

$$\begin{aligned} \min_{O,p} \quad & \left|\left| |\mathcal{F}(P(\mathbf{r}-\mathbf{R}_j)O(\mathbf{r}))| - \sqrt{I_j(\mathbf{k})} \right|\right|^2 + \alpha||p||_1. \\ \text{s.t.} \quad & p = O \end{aligned} \tag{14}$$

Results are given, for extrusions type defects, in the figure below, and the defect are better reconstructed when using the full knowledge of the prior object. Another interesting choice could be to look for a sparse reconstruction of the object around O_p, in which case the regularizer would be $||O - O_p||_1$, but this is not discussed in this paper.

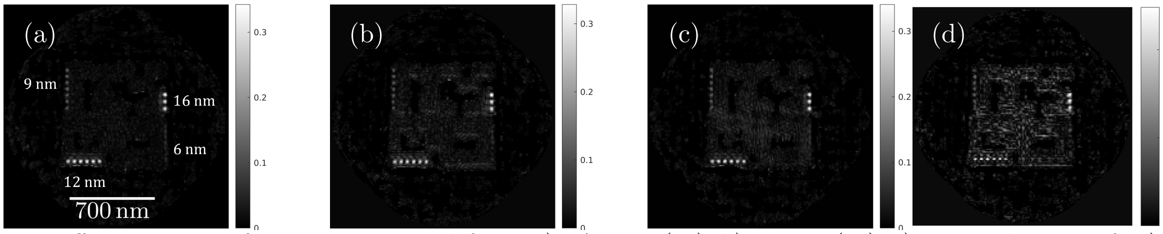

Figure 6: Difference images for extrusion type defects. a)MAP, Eq.(10), b)IR, Eq. (12), c) PIE with prior info,d) Lasso, Eq. (14).

3.5 Conclusions

We made use of ptychography to reconstruct the layout of patterned defective EUV masks. The inclusion of prior information enabled the imaging and detection of defects whose size is below the theoretical Abbe limit imposed by the NA. The combination of different update rules – stemming from the minimization of certain cost functionals – is found to further improve the quality of the inspection and to result in an increased defects' SNR under the assumption that the main source of the noise is dictated by the photon counting.

3.6 Acknowledgments

This project has received financial support from the European Union's Horizon 2020 research and innovation program under the Marie Skłodowska-Curie Grant Agreement No. 675745.

REFERENCES

[1] Erdmann, A., Evanschitzky, P., Mesilhy, H., Philipsen, V., Hendrickx, E., and Bauer, M., "Attenuated phase shift mask for extreme ultraviolet: can they mitigate three-dimensional mask effects?," *Journal of Micro/Nanolithography, MEMS, and MOEMS* **18**(1), 1 – 13 (2018).

[2] Rodenburg, J. M. and Faulkner, H. M. L., "A phase retrieval algorithm for shifting illumination," *Applied Physics Letters* **85**(20), 4795–4797 (2004).

[3] Maiden, A. M. and Rodenburg, J. M., "An improved ptychographical phase retrieval algorithm for diffractive imaging," *Ultramicroscopy* **109**(10), 1256 – 1262 (2009).

[4] Maiden, A., Johnson, D., and Li, P., "Further improvements to the ptychographical iterative engine," *Optica* **4**, 736–745 (Jul 2017).

[5] Thibault, P., Dierolf, M., Bunk, O., Menzel, A., and Pfeiffer, F., "Probe retrieval in ptychographic coherent diffractive imaging," *Ultramicroscopy* **109**(4), 338 – 343 (2009).

[6] Chang, H., Enfedaque, P., Zhang, J., Reinhardt, J., Enders, B., Yu, Y.-S., Shapiro, D., Schroer, C. G., Zeng, T., and Marchesini, S., "Advanced denoising for x-ray ptychography," *Opt. Express* **27**, 10395–10418 (Apr 2019).

[7] Konijnenberg, A. P., Coene, W. M. J., and Urbach, H. P., "Model-independent noise-robust extension of ptychography," *Opt. Express* **26**, 5857–5874 (Mar 2018).

[8] Yan, H., "Ptychographic phase retrieval by proximal algorithms," *New Journal of Physics* **22**, 023035 (feb 2020).

[9] Maiden, A. M., Humphry, M. J., and Rodenburg, J. M., "Ptychographic transmission microscopy in three dimensions using a multi-slice approach," *J. Opt. Soc. Am. A* **29**, 1606–1614 (Aug 2012).

[10] Dierolf, M., Menzel, A., Thibault, P., Schneider, P., Kewish, C., Wepf, R., Bunk, O., and Pfeiffer, F., "Ptychographic x-ray computed tomography at the nanoscale," *Nature* **467**, 436–9 (09 2010).

[11] Zheng, G., Horstmeyer, R., and Yang, C., "Wide-field, high-resolution fourier ptychographic microscopy (vol 7, pg 739, 2013)," *Nature Photonics* **9**, 621–621 (09 2015).

[12] Wakonig, K., Diaz, A., Bonnin, A., Stampanoni, M., Bergamaschi, A., Ihli, J., Guizar-Sicairos, M., and Menzel, A., "X-ray fourier ptychography," *Science Advances* **5**(2) (2019).

[13] Zhang, H., Jiang, S., Liao, J., Deng, J., Liu, J., Zhang, Y., and Zheng, G., "Near-field fourier ptychography: super-resolution phase retrieval via speckle illumination," *Opt. Express* **27**, 7498–7512 (Mar 2019).

[14] Gardner, D. F., Zhang, B., Seaberg, M. D., Martin, L. S., Adams, D. E., Salmassi, F., Gullikson, E., Kapteyn, H., and Murnane, M., "High numerical aperture reflection mode coherent diffraction microscopy using off-axis apertured illumination," *Opt. Express* **20**, 19050–19059 (Aug 2012).

[15] Porter, C. L., Tanksalvala, M., Gerrity, M., Miley, G., Zhang, X., Bevis, C., Shanblatt, E., Karl, R., Murnane, M. M., Adams, D. E., and Kapteyn, H. C., "General-purpose, wide field-of-view reflection imaging with a tabletop 13 nm light source," *Optica* **4**, 1552–1557 (Dec 2017).

[16] Helfenstein, P., Rajeev, R., Mochi, I., Kleibert, A., Vaz, C. A. F., and Ekinci, Y., "Beam drift and partial probe coherence effects in EUV reflective-mode coherent diffractive imaging," *Opt. Express* **26**, 12242–12256 (Apr 2018).

[17] Rajendran, R., Mochi, I., Helfenstein, P., Mohacsi, I., Redford, S., Mozzanica, A., Schmitt, B., Yoshitake, S., and Ekinci, Y., "Towards a stand-alone high-throughput EUV actinic photomask inspection tool: RESCAN," in [*Metrology, Inspection, and Process Control for Microlithography XXXI*], **10145**,, 199 – 210, International Society for Optics and Photonics, SPIE (2017).

[18] Mochi, I., Helfenstein, P., Rajeev, R., Fernandez, S., Kazazis, D., Yoshitake, S., and Ekinci, Y., "Actinic inspection of EUV reticles with arbitrary pattern design," in [*International Conference on Extreme Ultraviolet Lithography 2017*], **10450**,, 28 – 37, International Society for Optics and Photonics, SPIE (2017).

[19] Ansuinelli, P., Coene, W. M. J., and Urbach, H. P., "Improved ptychographic inspection of EUV reticles via inclusion of prior information," *Appl. Opt.* **59**(20), 5937–5947 (2020).

[20] Thibault, P. and Guizar-Sicairos, M., "Maximum-likelihood refinement for coherent diffractive imaging," *New Journal of Physics* **14**, 063004 (jun 2012).

[21] Xu, X., Konijnenberg, A. P., Pereira, S., and Urbach, H. P., "Phase retrieval of the full vectorial field applied to coherent Fourier scatterometry," *Optics Express* **25**(24), 29574–29586 (2017).

[22] van Beurden, M. C., "Fast convergence with spectral volume integral equation for crossed block-shaped gratings with improved material interface conditions," *J. Opt. Soc. Am. A* **28**, 2269–2278 (Nov 2011).

[23] van Beurden, M. C., "A spectral volume integral equation method for arbitrary bi-periodic gratings with explicit Fourier factorization," *Progress In Electromagnetics Research B* **36**, 133–149 (Nov 2012).

[24] Mochi, I., Goldberg, K. A., Fontaine, B. L., Tchikoulaeva, A., and Holfeld, C., "Actinic imaging of native and programmed defects on a full-field mask," in [*Extreme Ultraviolet (EUV) Lithography*], **7636**,, 425 – 433, International Society for Optics and Photonics, SPIE (2010).